Dynamics and transport properties of three surface quasigeostrophic point vortices

C. K. Taylor and Stefan G. Llewellyn Smith

Citation: Chaos **26**, 113117 (2016); doi: 10.1063/1.4967806
View online: http://dx.doi.org/10.1063/1.4967806
View Table of Contents: http://scitation.aip.org/content/aip/journal/chaos/26/11?ver=pdfcov
Published by the AIP Publishing

Dynamics and transport properties of three surface quasigeostrophic point vortices

C. K. Taylor and Stefan G. Llewellyn Smith[a)]
Department of Mechanical and Aerospace Engineering, Jacobs School of Engineering, University of California, San Diego, 9500 Gilman Drive, La Jolla, California 92093-0411, USA

(Received 25 May 2016; accepted 2 November 2016; published online 17 November 2016)

The surface quasi-geostrophic (SQG) equations are a model for low-Rossby number geophysical flows in which the dynamics are governed by potential temperature dynamics on the boundary. We examine point vortex solutions to this model as well as the chaotic flows induced by three point vortices. The chaotic transport induced by these flows is investigated using techniques of Poincaré maps and the Finite Time Braiding Exponent (FTBE). This chaotic transport is representative of the mixing in the flow, and these terms are used interchangeably in this work. Compared with point vortices in two-dimensional flow, the SQG vortices are found to produce flows with higher FTBE, indicating more mixing. Select results are presented for analyzing mixing for arbitrary vortex strengths. *Published by AIP Publishing*. [http://dx.doi.org/10.1063/1.4967806]

Gaining an understanding of mixing is important for many problems, from biomedical devices using micro-droplets to predicting pollutant dispersal over many kilometers in the atmosphere. In this work, we examine transport in a model of ocean flow at large scales to gain insight into mixing for these kinds of systems. Simple point vortices are used as a model system, and comparisons are also drawn between this model and the two-dimensional model where point vortices have been studied extensively. Recently developed tools for quantifying mixing are utilized in order to find trends and make comparisons.

I. INTRODUCTION

Many fields within the fluid dynamics community require a good understanding of mixing in order to advance in problems such as miniaturizing biomedical devices,[23] improving combustion engines,[1,30] and predicting how pollutants carried in the ocean or atmosphere will disperse.[12,16,20] While mixing is a familiar concept, the particulars of how to define and measure the extent of mixing in a given flow remain challenging. Mixing is generally decomposed into two stages, starting with the process of stirring, where diffusion is negligible but advection will stretch material lines into filaments.[29] The second stage begins when the scales of the filaments are small enough that the advection effects are of the same order as diffusion, and from there the mixed region will homogenize. The initial step of stirring was studied by Aref and Pomphrey under the name "chaotic motion" in the simplified case of point vortices in two-dimensional flow.[5] In this case, chaos refers to aperiodic behavior in which two points in the flow that are initially very near will exhibit very different trajectories over finite time.[4] Physically, a particle in the flow that undergoes chaotic advection will, over time, be carried through the entire region and interact with all of the fluid particles that are bounded by the same material lines. Thus, if dye is introduced into the fluid anywhere in that region, the dye will eventually spread over the entire region, satisfying the typical conceptual definition of mixing. This chaotic advection is what we consider to be mixing in this work. In their study of point vortices, Aref and Pomphrey found that three interacting vortices would follow regular trajectories, and four vortices could follow chaotic trajectories. The four vortex result also applies to the analysis of flow surrounding three vortices, because a point in the fluid can be modeled as a particle that is passively carried by the fluid, represented as a point vortex of zero strength. Thus, by Aref and Pomphrey's findings, three point vortices will follow periodic paths but can produce chaotic flow in the surrounding fluid.

This work examines point vortices and the resulting chaotic transport in the Quasigeostrophic (QG) approximation. This model approximates the ocean as a thin body of fluid spread over a rotating sphere and assumes the fluid is stratified, Boussinesq, and effectively inviscid at large scales. The equations of motion can be nondimensionalized using characteristic scales—velocity U, horizontal length L, height H, kinematic viscosity ν, Coriolis frequency f, and buoyancy frequency N—to obtain dimensionless numbers that characterize a regime of motion. Inviscid flow is characterized by high Reynolds number $Re = UL/\nu$, and in this regime the viscous stress is negligible and can be ignored in the equations of motion. The Rossby number, $Ro = U/fL$, compares the local velocity to the velocity of the rotating coordinates. In the limit $Ro \to 0$, the QG equations of motion are obtained. In the QG equations, potential vorticity, or the combined effects of vorticity, buoyancy, and the Coriolis force, is conserved. The Surface Quasigeostrophic (SQG) model[14] further simplifies the physics by specifying that the potential vorticity is zero in the interior so that the flow is determined by evolution of buoyancy on the boundaries. Physically, this can be pictured as motion induced by a buoyancy

[a)]sgls@ucsd.edu

distribution at the surface. As the buoyancy distribution evolves, the internal fluid must also evolve to satisfy zero potential vorticity.

At ocean mesoscales (flow with horizontal scales of 10–100 km), stratification and rotation both contribute to suppressing vertical motion. Thus, horizontal velocities dominate the dynamics, but flow will still vary in the vertical and have weak vertical velocity. This quasi-two-dimensional model presents an interesting challenge to classic tools for studying mixing. The flow does not require mixing measures that examine the full three-dimensional complexity, but neglecting the vertical dependence altogether would be overly simplified. Some researchers looking to understand mixing in this middle ground have considered kinematic models of eddies[22] or approximating three-dimensional shear with horizontal shear that varies in the vertical.[24] This work complements the current body of knowledge by examining dynamic models in this quasi-two-dimensional regime and using a global complexity measure to explore mixing in the model's parameter space.

By examining mixing for simple exact solutions in the SQG model, this work provides insight into mixing in the ocean as well as the comparison between these dynamics to those found in classical two-dimensional chaotic flows. Since vortices are characteristic structures in the ocean,[6,10] simplified point vortices provide an ideal model problem for studying mixing at the mesoscale. The article is structured as follows. In Section II, the point vortex solution to the SQG equations is reviewed in analogy with those for two-dimensional flow. In Section III, the evolution of three vortices is derived for equal vortex strengths. In Section IV, the transport properties of this flow are analyzed using the algorithms developed by Thiffeault and Budišić.[26] Section V calculates vortex interaction for arbitrary vortex strength and outlines the resulting mixing. Finally, a concluding discussion is given in Section VI.

II. POINT VORTEX MODEL

Classical (2D Euler) point vortices have been studied extensively in the examination of regular and chaotic trajectories.[4] The equations of motion are two-dimensional and inviscid,

$$\frac{D\vec{u}}{Dt} = 0\,, \quad \nabla \cdot \vec{u} = 0. \tag{1}$$

Written instead in terms of a streamfunction and vorticity (using the geophysical convention), the equations become

$$\Delta\psi = \omega, \tag{2}$$

where

$$\omega = \hat{z} \cdot (\nabla \times \vec{u}), \quad \nabla\psi = (v, -u), \tag{3}$$

and Δ is the two-dimensional Laplacian. In the two-dimensional case, the point vortex is defined by a singular point of vorticity, and thus the streamfunction is the free-space solution to

$$\Delta\psi_{2D} = -\kappa\delta(x - x_0)\delta(y - y_0) \tag{4}$$

for a point vortex of strength (or circulation) κ and position (x_0, y_0). The solution is the classic point vortex

$$\psi_{2D} = -\frac{\kappa}{2\pi}\log|\vec{x} - \vec{x}_0|. \tag{5}$$

For multiple point vortices with strengths κ_j and positions $\vec{x}_j$, the streamfunctions will be added and the vortices themselves will evolve according to

$$(\dot{x}_i, \dot{y}_i) = -\frac{1}{2\pi}\sum_j{}' \frac{\kappa_j}{|\vec{x}_i - \vec{x}_j|^2}(y_i - y_j, -x_i + x_j). \tag{6}$$

The SQG model presented by Held *et al.*[14] is derived from the QG equations for three-dimensional flow on a rotating planet, with the hydrostatic and *f*-plane approximations. These approximations are appropriate for mesoscale flow. In Cartesian geometry with rotation given by the Coriolis parameter, f, the equations are

$$\begin{aligned} Ro\frac{Du}{Dt} - v &= -\phi_x, \\ Ro\frac{Dv}{Dt} + u &= -\phi_y, \\ \theta &= \phi_z, \\ u_x + v_y + Ro\, w_z &= 0, \\ \frac{D\theta}{Dt} + w &= 0 \end{aligned} \tag{7}$$

with the conventional material derivative

$$\frac{D}{Dt} = \frac{\partial}{\partial t} + \vec{u} \cdot \nabla\,,$$

and where the variables (u, v, w) are the velocities in the (x, y, z) directions, respectively; ϕ is the geopotential height; and θ is the buoyancy. Geopotential height refers to the pressure surface compared to a reference height, usually sea level, given by

$$\phi = \frac{p - p_0}{\rho_0}.$$

Buoyancy is the force experienced by a fluid parcel due to differences between its density and the surrounding density,

$$\theta = -\frac{g(\rho' - \rho_0)}{\rho_0}.$$

The physical constants in the equations of motion are the Coriolis parameter, f, and the buoyancy frequency, N. An expansion in small $Ro \ll 1$ yields at $O(1)$[18,28]

$$\Delta\psi = q, \quad \psi^s_z = \theta^s, \quad \frac{Dq}{Dt} = 0, \tag{8}$$

where Δ is the three-dimensional Laplacian, q is the potential vorticity, the superscript s indicates that the variable is evaluated at the surface of the domain (conventionally $z = 0$), and the subscript z indicates the z-derivative. The SQG model is

(8) with the more restrictive and dynamically consistent condition that $q=0$ in the interior.

While the 2D Euler system is governed by the specified vorticity, in SQG flow the system is governed instead by the temperature at the surface. Thus, the analogous point vortex flow in SQG is found from the definition

$$\theta^s = \kappa\delta(x-x_0)\delta(y-y_0). \tag{9}$$

The solution to (8) is

$$\psi = -\frac{\kappa}{2\pi}\frac{1}{|\vec{x}-\vec{x}_0|}, \tag{10}$$

given in the study of Held *et al.*[14] Note that, unlike the 2D case, this solution has three-dimensional dependence. For an arbitrary number of vortices with strengths κ_j and positions $\vec{x}_j$, i.e.,

$$\Delta\psi = 0\,, \quad \psi_z^s = \sum_j \kappa_j\delta(x-x_j)\delta(y-y_j), \tag{11}$$

the solution is the linear combination

$$\psi = -\frac{1}{2\pi}\sum_j \frac{\kappa_j}{|\vec{x}-\vec{x}_j|}. \tag{12}$$

The point vortices themselves will be advected by the flow, neglecting the singular velocity contribution of each point vortex at its own location. From conservation of energy in (7), w is of order Ro and so is neglected in (8). Each vortex then induces only horizontal motion, so the vertical position of each vortex will remain constant. In this work, we consider all vortices to be on the same plane, $z=0$. The horizontal evolution of a given point vortex is determined by the sum of contributions of every other vortex in the system, given by

$$(\dot{x}_i,\dot{y}_i) = -\frac{1}{2\pi}{\sum_j}' \frac{\kappa_j}{|\vec{x}_i-\vec{x}_j|^3}(y_i-y_j,-x_i+x_j), \tag{13}$$

where the prime indicates that the self-interaction $i=j$ is ignored. The difference between the dynamics of 2D and SQG point vortices is essentially the powers of vortex separation in the denominator appearing in (5) and (6) for the classical case and appearing in (12) and (13) in the SQG case. The power in the SQG case is greater by 1. On the surface, at $z=0$, this is the only difference. However, in the SQG case, all fields including streamfunction are a function of depth, z, that appears parametrically in (12). The advection equation (13) however does not lead to any change in z for trajectories.

III. THREE VORTEX CASE

As detailed in Aref's 1983 review,[4] for planar two-dimensional flow, three point vortices are the minimum number that produce chaotic flow. The three vortices will evolve in a regular pattern, but a passive particle (a vortex of strength 0) will follow a chaotic trajectory for certain vortex and initial particle positions. Aref's analysis is based solely on Hamiltonian mechanics, and thus applies to SQG as well. Thus, to study chaos in SQG, we consider three SQG point vortices.

To analyze the vortex interaction, we extend the analysis of Kuznetsov and Zaslavsky[15] for classical point vortices of equal strength. If all vortices have equal strength, the strength can be absorbed into the length scales and eliminated from the nondimensional equations. Kuznetsov and Zaslavksy consider the position of each vortex as a complex number, $z_j = x_j + iy_j$ (not to be confused with the vertical coordinate z), and relocate the origin to the center of vorticity, given by

$$\frac{\sum_j \kappa_j|z_j|^2}{\sum_j \kappa_j}.$$

Then, they write the vortex positions in terms of action variables J_n, θ_n,

$$z_j = \frac{1}{\sqrt{3}}\sum_{n=1}^{2}\sqrt{2J_n}\,e^{i\theta_n}\,e^{-2i\pi n(j-1)/3} \quad j=1,\ldots,3. \tag{14}$$

From here, make another change of variables

$$\begin{aligned} I_1 &= J_2 - J_1, \quad I_2 = J_2 + J_1, \\ \phi_1 &= \theta_2 - \theta_1, \quad \phi_2 = \theta_2 + \theta_1. \end{aligned} \tag{15}$$

These new variables I_1 and I_2 have geometric significance, with

$$I_1 = A/\sqrt{3}\,, \quad I_2 = L^2/4, \tag{16}$$

where A represents the signed area of the triangle formed by the vortex positions and $L^2 = \sum \kappa_j|z_j|^2$ is the angular momentum, a constant.

The vortex dynamics can then be analyzed by taking advantage of the Hamiltonian relations

$$\dot{I}_1 = \frac{\partial H}{\partial\phi_1}, \qquad \dot{I}_2 = -\frac{\partial H}{\partial\phi_2}, \tag{17}$$

where the Hamiltonian H is the energy of the system, a constant of motion, given by

$$H = \frac{1}{4\pi}\sum_i\sum_j \frac{1}{|z_i-z_j|}. \tag{18}$$

Finally, define the "area variable" as

$$I = \left(\frac{I_1}{I_2}\right)^2 = 16A^2/3L^4. \tag{19}$$

Because H and I_2 are constants, the evolution of I depends only on I. A potential function is defined as $-\dot{I}^2$ such that where this potential is negative the solution is real, and thus the plotted curve of $\dot{I}^2(I)$ can be interpreted as a potential well. These potential curves are shown in Figure 1 for various energies. There are two regimes of motion visible, separated by the critical energy labeled H_c. In the higher energy

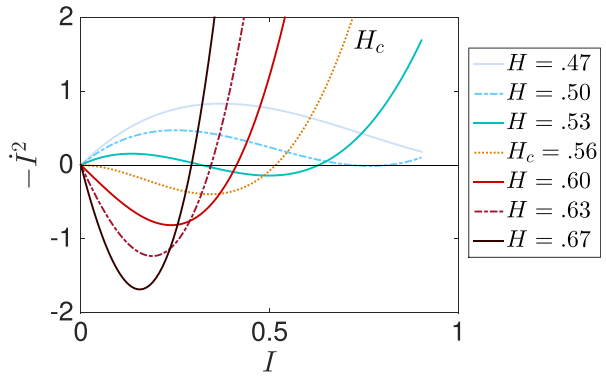

FIG. 1. Potential function $-\dot{I}^2(I)$ showing the evolution of vortex motion for various energies, H. There is a critical energy $H_c = 0.5623$, marked as a dotted line, that divides the two regimes of motion.

regime, two of the vortices are close enough that they will orbit one another, while the vortex further away remains separate. In the other regime of motion, all three vortices will orbit one another. The form of H and the quantitative shape of the curves in Figure 1 is the only formal difference with the analysis of Aref. The resulting dynamics of the vortices is qualitatively similar.

These potential wells can be used to determine the period of motion from the integral

$$T = 2\int_{I_{\min}}^{I_{\max}} \frac{dI}{|\dot{I}|}, \tag{20}$$

where $I_{\min}$ and $I_{\max}$ refer to the intersections of the well with the $-\dot{I}^2 = 0$ axis, and the factor of 2 is needed to account for the return from $I_{\max}$ to $I_{\min}$ over one cycle. After one cycle, I will return to its original value, meaning the vortex triangle has its original area, but the vortices will be permuted among the triangle vertices. This can be seen clearly in the co-rotating frame (explained below) in Figure 2, where in (a) all three vortices orbit and in (b) only two vortices are orbiting. At time T, the area has returned to its original value, but the

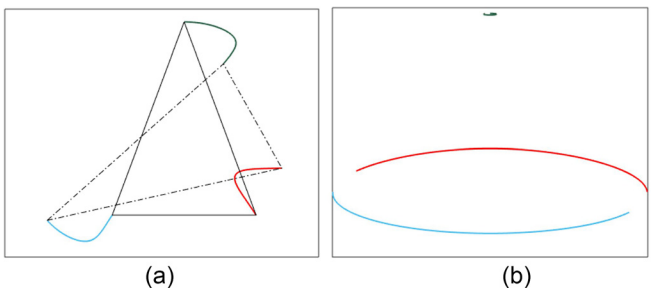

FIG. 2. Equal strength vortex trajectories in the co-rotating frame (a) up to and (b) just before time T, demonstrating the necessary factors for computing T_v in (21). For (a) the lower-energy three-vortex orbits, a triangle connecting the vortices at $t = 0$ (solid) and $t = T$ (dotted-dashed) is also shown. The two triangles are equivalent, but the vortex associated with each vertex has changed, therefore requiring a factor of 3 to return each vortex to its original position. For (b) the higher-energy two-vortex orbit, the trajectories are shown for a time just less than T to more clearly show the dynamics. The vortex that remains separate is about to return to its original position, but the two orbiting vortices will have changed positions. Therefore, this regime requires a factor of 2 to return each vortex to its original position.

orbiting vortices have changed positions. A higher energy results from two of the vortices orbiting at close range, so the period of vortex motion at higher values of H will be the area variable period T multiplied by an additional factor of 2. Then, for lower energies the three vortices will permute with one another; thus, the period of vortex motion will be T multiplied by an additional factor of 3.

$$T_v = \begin{cases} 3T & \text{if } H < H_c \\ 2T & \text{if } H > H_c. \end{cases} \tag{21}$$

The dependence of T_v on H across both regimes of motion is shown in Figure 3. Note the singularity at the boundary between the two regimes motion, $H = H_c = 0.5623$. Referring to Figure 1, it can be seen that the H_c potential well has a decaying approach to $I_{\min} = 0$, implying that the solution will take infinitely long to reach this turning point in I, thus resulting in the singularity in T_v exhibited in Figure 3.

Figure 4 also reveals that the vortices slowly rotate about their center of vorticity. The presence of a rotation becomes clear when z_j is written in terms of the new variables.

$$z_j(t) = \frac{L}{\sqrt{6}} e^{i\phi_2(t)/2}\Big[\left(1 - I^{1/2}(t)\right)^{1/2} e^{-2\pi i(j-1)/3} e^{-i\phi_1(t)/2} + \left(1 + I^{1/2}(t)\right)^{1/2} e^{-4\pi i(j-1)/3} e^{i\phi_1(t)/2}\Big]. \tag{20}$$

Note that at $t = 0$ and $t = T_v$, the term in the brackets is equal. Therefore, at $t = T_v$, each vortex has returned to its original position with a rotation about the center of vorticity of $\phi_2(T_v)/2$. This rotation can be calculated in a similar manner to the period of motion. Using

$$\dot{\phi}_2 = -\frac{\partial H}{\partial I_2}, \tag{23}$$

we find

$$\phi_2(T_v) = 2\int_{I_{\min}}^{I_{\max}} \frac{\dot{\phi}_2}{|\dot{I}|} dI. \tag{24}$$

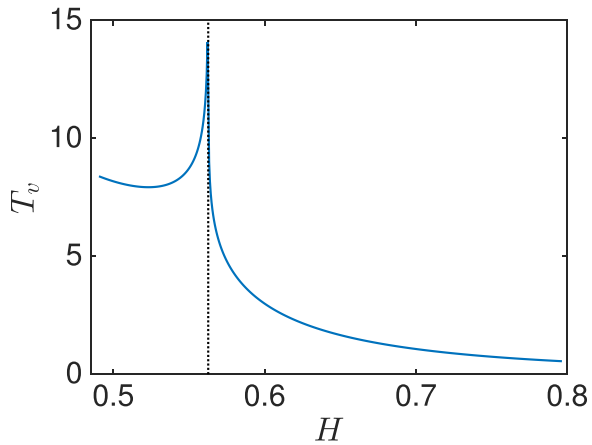

FIG. 3. Period of motion for each vortex T_v vs. H. The vertical dotted line shows the boundary between the two regimes of motion.

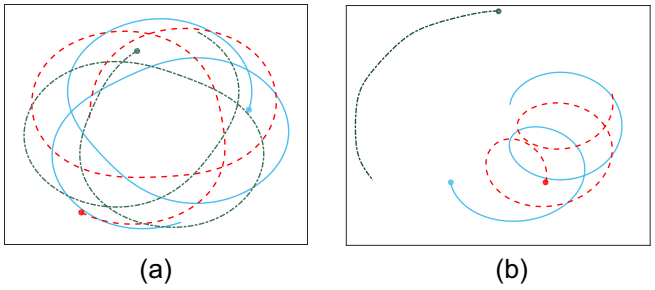

FIG. 4. Two regimes of motion are observed, (a) lower-energy two-vortex orbits and (b) higher-energy three-vortex orbits. The points indicate initial positions of vortices and the lines indicate trajectories in time. It is observed that the vortices permute and also rotate in time, resulting in braid-like trajectories.

With this shift, the motion of the vortices is described in its entirety. Vortex trajectories in the co-rotating frame are shown in Figure 5. For these plots and Section IV, we have normalized the horizontal coordinates by L.

IV. TRANSPORT

Using a standard ODE solver, the system of evolution equations (13) can be solved for any vortex distribution and initial passive particle position. If the resulting trajectories are strobed at every period of vortex motion and the frame is rotated to remove the vortex shifting, Poincaré maps such as those shown in Figure 6 are obtained. These can be compared to the two-dimensional Poincaré maps given in the first figure in Kuznetsov and Zaslavsky.[15]

It can be seen in Figure 6 that, while the dynamics are purely two-dimensional, the flow has vertical dependence. Even when particles follow regular trajectories (a)–(c), the trajectories change with depth. In the case where mixing is exhibited, the barriers of chaotic motion seem to extend as three-dimensional surfaces, and islands are observed at a range of depths. A three-dimensional visualization of the chaotic mixing is shown in Figure 7, and the islands are shown to extend in depth. This figure was produced by using a set of Poincaré sections to approximate the three-dimensional

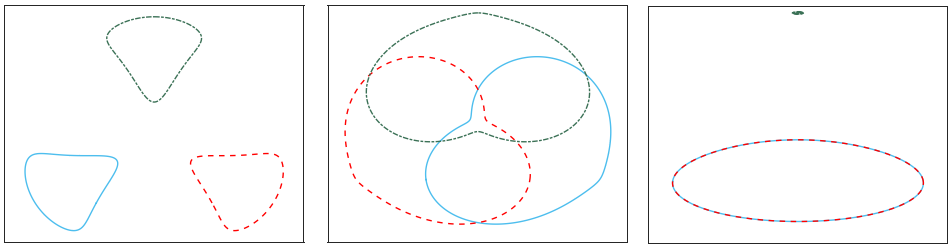

FIG. 5. Vortex trajectories for $H =$ (a) 0.54, (b) 0.56, and (c) 0.58 in the co-rotating frame. These demonstrate the two regimes of motion from Figure 1.

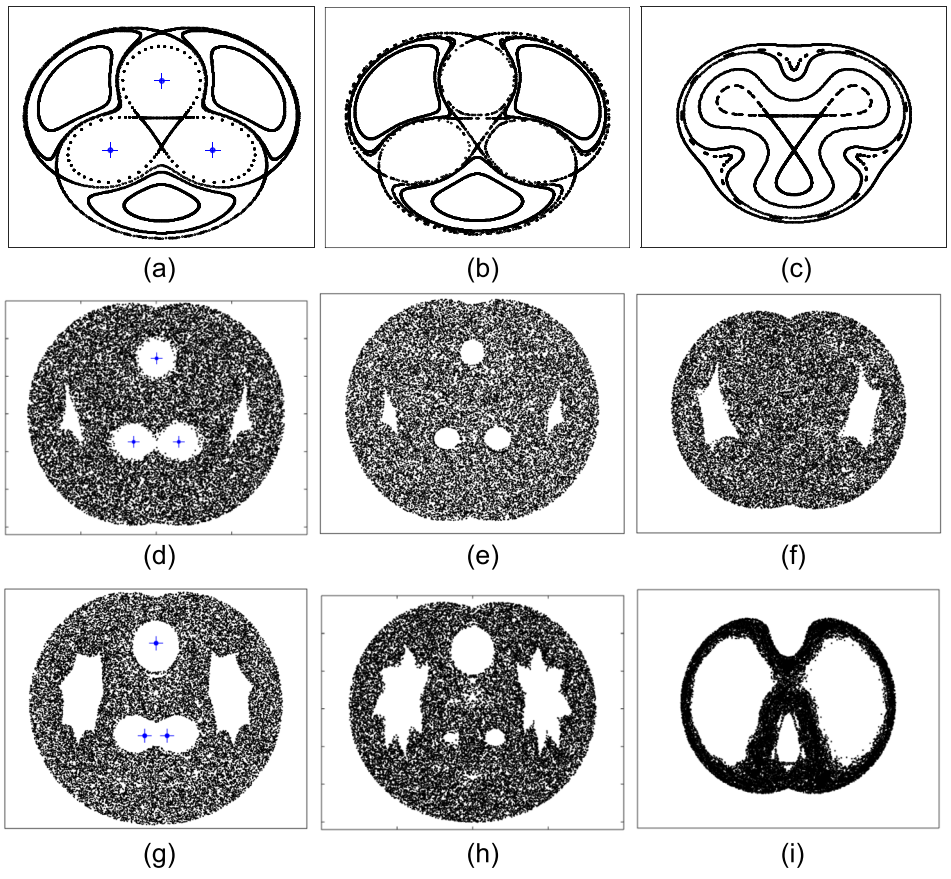

FIG. 6. Poincaré maps for SQG point vortices for two distinct vortex configurations sampled at three depths. Vortex positions are designated by blue crosses at the surface in (a) and (d). The upper row shows a non-mixing case, and it is observed that the paths change with depth. The lower row is a case where two vortices orbit one another, and this induces mixing, even at depth, though the chaotic region changes with depth. Compare the $z = 0$ plots (a) and (d) to classical solutions in Kuznetsov and Zaslavsky.[15]

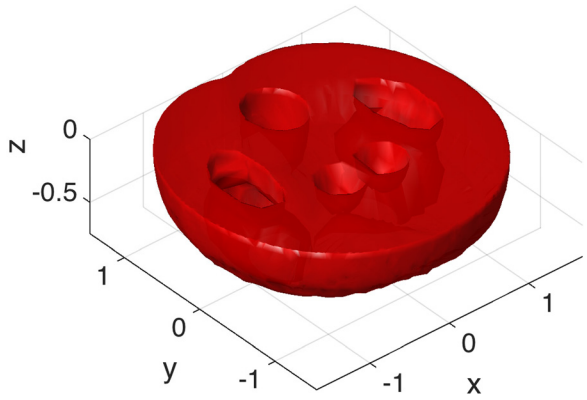

FIG. 7. A 3D visualization of the chaotic mixing region of a flow, demonstrating that the islands in the Poincaré maps extend as surfaces in three dimensions. This figure was produced by using a set of Poincaré sections to approximate the three-dimensional chaotic region, then using the MATLAB function alphavol[17] to produce the surface containing this region.

chaotic region, and approximating the surface of this volume using the MATLAB function alphavol.[17] Two islands near $(x, y) = (\pm 0.2, -0.5)$ descend only partway, whereas islands near $(x, y) = (\pm 1, 0)$ descend at least as far as was sampled here.

In order to analyze the quantitative effect of changing the vortex distribution (i.e., the parameter H) and compare the SQG vortices to two-dimensional vortices, it is necessary to use a measurable property. In chaotic advection, the relevant property is the complexity of the flow, and one of the most convenient measures of global complexity seems to be topological entropy. Informally, the topological entropy of a dynamical system measures the loss of information under the dynamics. The relation between topological entropy and maximal rate of stretching of material lines has been investigated by a number of authors.[19,25] It is useful in the context of mixing (or rather stirring), given the extensive study of the relation between material line stretching and transport. However, the value of topological entropy can be difficult to compute given only a velocity field.[7,19] Another tool that has been used to investigate chaotic advection are braids. These mathematical objects encode the topological entanglement of trajectories of 2D flows and have been used to investigate chaotic advection, for instance in the case of point vortices[9] and other flows.[8,25] Thiffeault and Budišić, based on earlier work,[25] have recently developed a tool called Braidlab that, among other functions, calculates the Finite Time Braiding Exponent (FTBE), which approximates topological entropy using particle trajectories.[11,26] The FTBE has been used in a detailed analysis of mixing in vortices.[27] The entropy of a braid of any set of trajectories from the flow is only a lower bound for the topological entropy of the flow although there is evidence that this bound can be made arbitrarily tight. Similarly, FTBE calculations based on aperiodic trajectories (of the sort computed in this paper) approximate the topological entropy of the flow.

One benefit of FTBE over the more commonly used Finite Time Lyapunov Exponent (FTLE)[21] is that FTBE provides a global measure of complexity as opposed to a local one,[2] allowing us to compare quantitatively the extent of

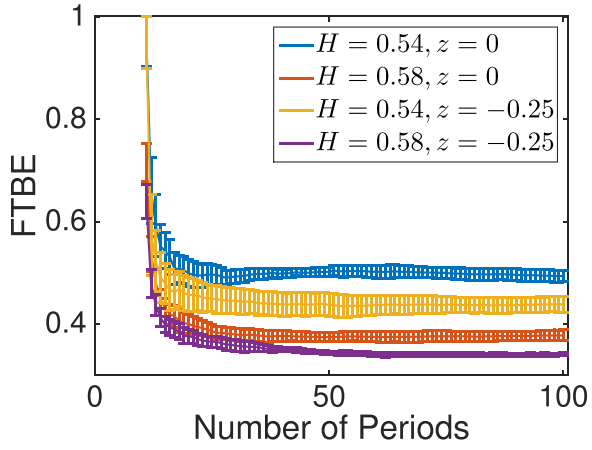

FIG. 8. Convergence of FTBE as integration time is increased.

stirring exhibited by different flows and thus explore the parameter space. This is particularly relevant when information is available only from a limited number of trajectories. (It is true that FTLEs could be used to generate a global measure by averaging over the spatial domain, but we pursue the FTBE approach here.)

The FTBE is dependent on the number of trajectories. While it also depends on the length of integration time, we found that it converged after enough time, as shown in Figure 8. Hence, we fix our analysis to include 64 trajectories integrated over 90 periods of vortex motion. As an estimate, the FTBE also varies slightly according to the time step chosen and the initial conditions of the trajectories. To quantify this variation, 13 different sets of 64 trajectories were used to generate a mean FTBE and standard deviation for each flow considered. Because the vortices are of equal strength and we have fixed $L = 1$, the only varying parameter is H.

FTBE vs. H is shown in Figure 9. The boundary between the two mixing regimes of vortex motion is indicated with the vertical dotted line, and it seems that for the lower-energy flows the observed mixing is relatively constant, with a minimum seen right at this regime boundary. Then, as the energy of the vortex configuration increases into the two-orbiting-vortices regime, we see FTBE increasing as well. Comparing the SQG case in Figure 9(a) to the classical two-dimensional case in Figure 9(b), the same qualitative trends are observed but the SQG case exhibits a higher level of mixing than the classical case. Finally, in Figure 9(c) FTBE is calculated at increasing depth, where the plane of vortex motion is $z = 0$. While the vortices still produce mixing at a depth close to the surface, the FTBE falls steeply at depths below approximately $z = -0.25$. This is consistent with qualitatively simpler Poincaré maps generated at depth $z = -0.5$ shown in Figure 6(f).

V. ARBITRARY VORTEX STRENGTH

Aref described the motion of three classical vortices of arbitrary strength by noting that these sums are constants of motion

$$\sum_i \kappa_i x_i, \quad \sum_i \kappa_i y_i, \quad \sum_i \kappa_i (x_i^2 + y_i^2),$$

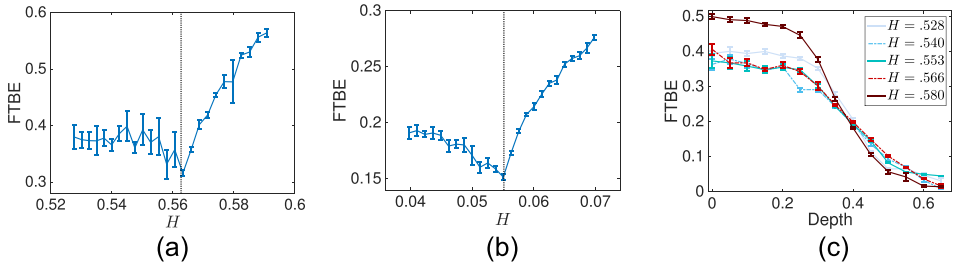

FIG. 9. For three equal strength SQG vortices, the FTBE is calculated for various vortex configurations characterized by the Hamiltonian, H, plotted (a) at the surface and (c) versus depth. For comparison, the FTBE for three equal strength two-dimensional vortices is shown in (b). Error bars of the FTBE are determined by statistical analysis of several choices of trajectory subsets. The vertical dotted line indicates the boundary between the two regimes of vortex motion.

and therefore the sum

$$\frac{1}{2}\sum_{i,j}\kappa_i\kappa_j l_{ij}^2, \qquad l_{ij}=|z_i-z_j|,$$

is constant and independent of the choice of coordinates. Additionally, the Hamiltonian is a constant. With the convention $\kappa_1\geq\kappa_2>0$, the above can be used to define a constant parameter C such that

$$\kappa_1\kappa_2 l_{12}^2+\kappa_2\kappa_3 l_{23}^2+\kappa_3\kappa_1 l_{13}^2=3\kappa_1\kappa_2\kappa_3 C.$$

C is essentially a time scale for relative motion. Note that, with the origin defined as the center of vorticity,

$$L=3\frac{\prod_j\kappa_j}{\sum_j\kappa_j}C,$$

so fixing $L=1$ in the equal strength case is equivalent to $C=1$.

For nonzero C we can define trilinear coordinates

$$b_1=\frac{l_{23}^2}{\kappa_1 C}, \quad b_2=\frac{l_{13}^2}{\kappa_2 C}, \quad b_3=\frac{l_{12}^2}{\kappa_3 C},$$

with

$$b_1+b_2+b_3=3.$$

Additionally, the physical regime is where the vortex positions can form a triangle, which in trilinear coordinates is expressed as

$$(\kappa_1 b_1)^2+(\kappa_2 b_2)^2+(\kappa_3 b_3)^2 \leq 2(\kappa_1\kappa_2 b_1 b_2+\kappa_2\kappa_3 b_2 b_3+\kappa_1\kappa_3 b_1 b_3).$$

From here, the SQG analysis differs from Aref's because we introduce the SQG Hamiltonian

$$H=\frac{1}{4\pi}{\sum_{i,j}}'\frac{\kappa_i\kappa_j}{l_{i,j}}.$$

Rewriting in terms of trilinear coordinates we find

$$H=\frac{\kappa_1\kappa_2\kappa_3}{2\pi|C|^{1/2}}\left(\frac{1}{|b_1\kappa_1|^{1/2}\kappa_1}+\frac{1}{|b_2\kappa_2|^{1/2}\kappa_2}+\frac{1}{|b_3\kappa_3|^{1/2}\kappa_3}\right), \tag{25}$$

$$\frac{1}{|b_1\kappa_1|^{1/2}\kappa_1}+\frac{1}{|b_2\kappa_2|^{1/2}\kappa_2}+\frac{1}{|b_3\kappa_3|^{1/2}\kappa_3}=\frac{2\pi H|C|^{1/2}}{g^3}=\theta, \tag{26}$$

where $g=(\kappa_1\kappa_2\kappa_3)^{1/3}$ is the geometric mean. The second line indicates a constant of motion that defines the phase trajectories in trilinear coordinates, and this constant θ is considered to be a shape parameter.

A particular set of vortex properties will correspond to a point in the plane of trilinear coordinates within the physical regime (see Figure 10). As time evolves, the vortices will trace the phase trajectory line. If the trajectory goes off to infinity, as in plot (c), the vortices scatter. Intersections of the trajectories with the physical regime boundary are points where the vortices are collinear. At the fixed points of the trajectories, which are at the center of the concentric curves in plots (a) and (b) and at trajectory intersections in plots (c) and (d), the vortices exhibit rigid motion. As for classical two-dimensional point vortices, this fixed point is

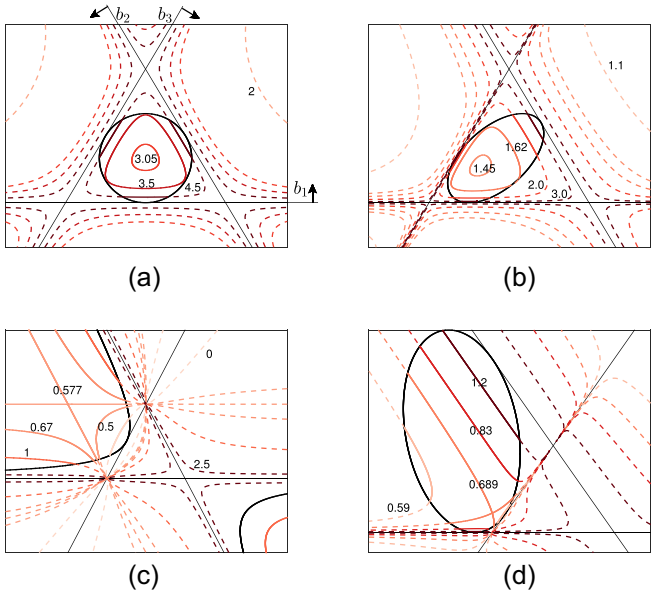

FIG. 10. Phase trajectories for various vortex strengths, with values of the shape parameter θ of each curve labeled. Three axes represent trilinear coordinates and the black curve shows the physical regime boundary. Compare to Figures 2, 3, and 4 in Aref.[3] Intersections of trajectories with physical regime boundaries represent collinear vortex configurations, escapes to infinity represent vortex scattering, and fixed points correspond to rigid motion of the vortex configuration.

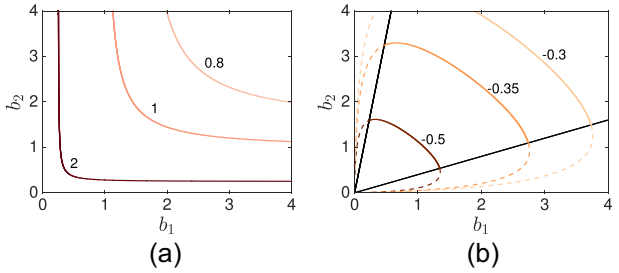

FIG. 11. Phase trajectories for the case $C = 0$ and two vortex strength combinations. The axes represent b_1, b_2 with $b_3 = -b_1 - b_2$, and the black lines show the physical regime boundary. Values of the shape parameter θ are labeled. In the case of (a), the physical regime boundaries lie along the (b_1, b_2) axes. Compare to Figures 5 and 6 in Aref.[3].

$$\left(b_1^\star, b_2^\star, b_3^\star\right) = \frac{1}{h}\left(\frac{1}{\kappa_1}, \frac{1}{\kappa_2}, \frac{1}{\kappa_3}\right), \tag{27}$$

where

$$h = \frac{1}{3}\left(\frac{1}{\kappa_1} + \frac{1}{\kappa_2} + \frac{1}{\kappa_3}\right)$$

is the harmonic mean.

If C is zero, the analysis is much the same with the change

$$b_1 = \frac{l_{23}^2}{\kappa_1}, \quad b_2 = \frac{l_{13}^2}{\kappa_2}, \quad b_3 = \frac{l_{12}^2}{\kappa_3},$$
$$b_1 + b_2 + b_3 = 0\,.$$

Expressed in terms of only (b_1, b_2), the trajectories will be given by

$$\frac{1}{|b_1\kappa_1|^{1/2}\kappa_1} + \frac{1}{|b_2\kappa_2|^{1/2}\kappa_2} + \frac{1}{|(b_1+b_2)\kappa_3|^{1/2}\kappa_3} = \theta,$$

as shown in Figure 11. Unlike the equal strength case, for arbitrary strength vortices the trajectory cannot be written explicitly, but the period of permutation and the rotation rate of the vortices can be computed from the resulting integration. Some examples of resulting vortex trajectories are shown in Figure 12.

From the phase trajectories in Figure 10, it is clear that 5 constants must be designated to specify one unique solution: three vortex strengths define the phase space, θ defines a particular phase trajectory, and C defines the time scale of following that trajectory. This parameter space is therefore very large, and as a preliminary examination only select slices are considered here. The integration time was also limited to only 60 periods of vortex motion.

First, the effect of varying L in the equal strength case is examined in Figure 13. It is clear from these results that changing L will vary the critical depth at which the FTBE drops steeply. Additionally, L affects the scale of the FTBE, where smaller L leads to overall higher FTBE. Small L implies that the vortices are spaced very near one another, resulting in larger velocity magnitudes in the flow between the vortices. It is perhaps not surprising that these higher velocities lead to more efficient mixing.

For a second case, the three initial distances between vortices are designated as $l_{13} = l_{12} = 2l_{23} = 0.2$ and the vortex strengths are constrained by $\kappa_1 = \kappa_2$. With this it is possible to solve for both these strengths as well as the third vortex strength from specifying two constants of motion. The parameter domain was chosen to be extensive, $-100 < \theta < 100$, $-1 < C < 1$, and a grid of 256 samples was examined. For these calculations, horizontal lengths are not normalized by L, as this results in changing C. All the simulations exhibited mixing, and the resulting FTBEs across this coarse grid are shown in Figure 14. Although only preliminary, the results seem to indicate a line in θ-C space of maximum FTBE. A more rigorous computational exploration of the parameter space would be needed to fully uncover the trends in FTBE.

As a third case, the constant of motion C is fixed as unity as it was in the equal strength case, and the vortex strengths are constrained by $\kappa_1 = \kappa_2 = 1$. Then, the system is determined by the θ-κ_3 parameter space. Based on phase trajectory plots, a representative parameter domain was chosen to be $-2 < \theta < 5$, $-8 < \kappa_3 < 8$. In this case, many parameter gridpoints did not have mixing, either because there was not a physical solution (marked as negative and separated by a black contour in Figure 14(b)), or because the solution resulted in two vortices orbiting so energetically as to dominate the dynamics, resulting in periodic flow trajectories (marked as zeros).

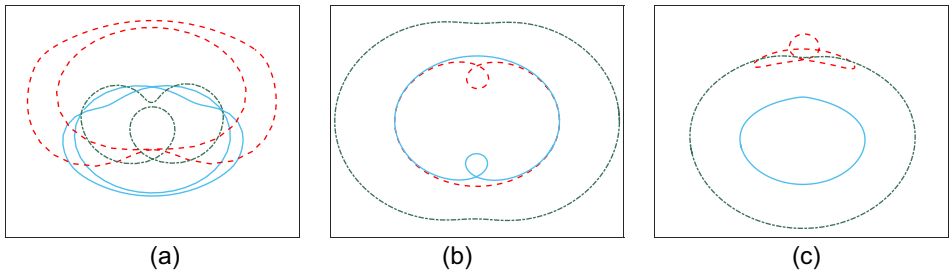

FIG. 12. Select examples of vortex trajectories. In (b) and (c), the shape parameter θ is near the unstable fixed point of the phase trajectories. In (b) specifically, the value of θ is slightly less than that of the critical phase trajectory shown in Figure 10(c), such that this phase trajectory will curve away from the unstable fixed point toward the trilinear axes. This vortex trajectory traces the phase trajectory back and forth between the intersections with the physical regime boundary, at which points the vortices are collinear. Similarly, in (c), this physical trajectory represents the phase trajectory in Figure 10(d) that traces from the intersection near the top of oval that is the physical regime boundary, passes near the unstable fixed point, and then traces to the intersection near the right of the oval.

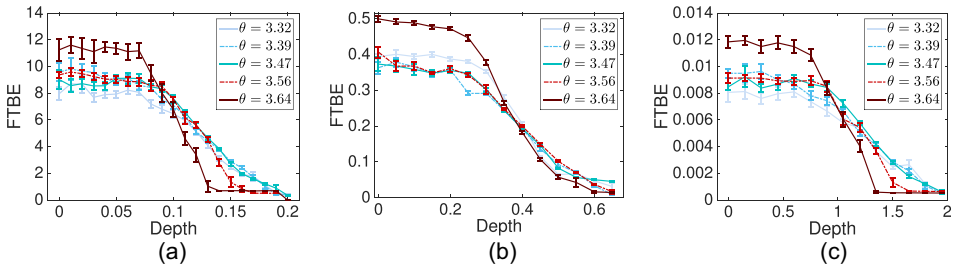

FIG. 13. Comparing the $O(1)$ equal strength point vortex solutions of FTBE vs. depth under changes to L. These plots show there is a critical depth beyond which the FTBE decreases sharply. For (b) $L = 1$ the critical depth appears to be $z = -0.25$, and increasing Ro increases the drop-off of FTBE for higher energies. For (a) $L = 0.1$, the critical depth has decreased to $z = -0.075$, and mixing has increased. For (c) $L = 10$, the critical depth has increased to $z = -0.75$, and mixing has decreased.

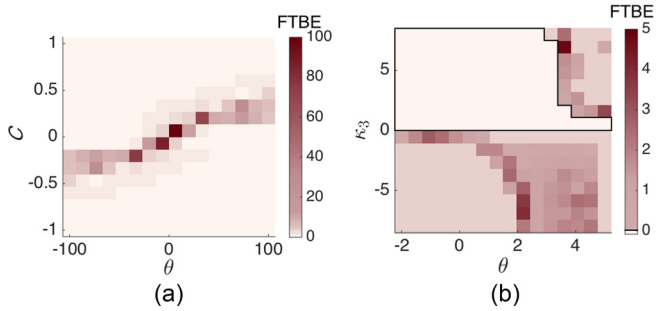

FIG. 14. Coarse FTBE results for arbitrary vortex strength cases shown for (a) the θ-C parameter space where the initial configuration is fixed and $\kappa_1 = \kappa_2$, and (b) the θ-κ_3 parameter space where $\kappa_1 = \kappa_2 = 1$ and $C = 1$. Negative FTBE represent nonphysical solutions, also separated by a black contour, whereas zero FTBE is physical but not energetic enough to induce mixing.

VI. SUMMARY AND CONCLUSION

This work has presented a novel analysis of SQG point vortex interaction as well as an exploration of the surrounding flow properties. As in the two-dimensional case, three vortices have the potential to induce chaos in the surrounding flow trajectories. This mixing has been diagnosed using the classical tool of Poincaré maps and the new FTBE tool. These vortices behave qualitatively in the same way as classical two-dimensional point vortices, exhibiting the same two regimes of motion in the equation strength case, and similar phase trajectories in the arbitrary strength cases.

The FTBE seems to provide a good measure of global complexity, revealing quantitative trends in mixing based on the flow parameters. While the value of the FTBE is not meant to be construed as a physical value, it can be used to compare relative tracer complexity between flows, where a higher FTBE indicates higher complexity and thus mixing. The first trend observed for SQG point vortex flows is that the FTBE is relatively constant in the regime of three orbiting vortices, then a minimum is found near the regime boundary, and mixing then increases with energy in the regime of two orbiting vortices. Also, the SQG case exhibits a higher extent of mixing than the classical two-dimensional case. The second trend is that there is a critical depth below which the FTBE falls steeply, and this depth is dependent on the constant of motion $L = \sum_i \kappa_i |z_i|^2$. Finally, a third trend is given in a preliminary investigation of FTBE for arbitrary vortex strength, which seems to indicate a line in θ-C space that corresponds to maximum mixing.

Work in progress will expand on this analysis to determine the effect of including $O(Ro)$ velocities. Following others, Muraki *et al.*[18] have calculated the small Ro-order expansion to the QG equations. The $O(Ro)$ equations include derivatives of the $O(1)$ solution, and in the point vortex case, where the $O(1)$ solution is singular, these terms are very problematic. However, the vertical velocity can instead be obtained from the energy conservation equation

$$w + \frac{D\theta}{Dt} = 0.$$

It is thus possible to examine the effect of vertical velocity on mixing, though in this case the solution is not dynamically consistent because the velocity is not divergenceless. For a dynamically consistent solution, a different model problem must be used. Other ongoing work is examining mixing due to elliptic patches formed by collapsed constant-PV ellipsoids, as in the study of Dritschel *et al.*[13]

Because the SQG model is relevant to large-scale ocean flows, understanding mixing in this model should provide insights into the physical processes behind pollution dispersion or vehicle trajectories in weakly three-dimensional flows. As a two-dimensional model with vertical dependence, such examination also shows how tools for studying mixing in two-dimensional flow can be modified to apply to more complicated, three-dimensional problems. While the FTBE cannot be extended directly to three dimensions, the relative scales of vertical to horizontal motion mean that the topological properties of the flow used by the FTBE are still two-dimensional to leading order.

ACKNOWLEDGMENTS

This work was funded by the *Ocean 3D+1* Office of Naval Research Multiple University Research Initiative. Special thanks to Marko Budišić for his help using Braidlab and to Drew Poje for fruitful discussions.

[1]G. H. Abd-Alla, Energy Convers. Manage. **43**, 1027 (2002).
[2]M. R. Allshouse and T. Peacock, Chaos **25**, 097617 (2015).
[3]H. Aref, Phys. Fluids **22**, 393 (1979).
[4]H. Aref, Annu. Rev. Fluid Mech. **15**, 345 (1983).
[5]H. Aref and N. Pomphrey, Phys. Lett. **78A**, 297 (1980).
[6]D. L. Bartels and R. A. Maddox, Mon. Weather Rev. **119**, 104 (1991).
[7]R. Bowen, Trans. Am. Math. Soc. **184**, 125 (1973).
[8]P. L. Boyland, H. Aref, and M. A. Stremler, J. Fluid Mech. **403**, 277 (2000).
[9]P. L. Boyland, M. A. Stremler, and H. Aref, Physica D **175**, 69 (2003).

[10]F. P. Bretherton and M. Karweit, *Numerical Models of Ocean Circulation* (National Academy of Sciences, 1975), pp. 237–249.
[11]M. Budišić and J.-L. Thiffeault, Chaos **25**, 087407 (2015).
[12]C. Coulliette, F. Lekien, J. D. Paduan, G. Haller, and J. E. Marsden, Environ. Sci. Technol. **41**, 6562 (2007).
[13]D. G. Dritschel, J. N. Reinaud, and W. J. McKiver, J. Fluid. Mech. **505**, 201 (2004).
[14]I. M. Held, R. T. Pierrehumbert, S. T. Garner, and K. L. Swanson, J. Fluid Mech. **282**, 1 (1995).
[15]L. Kuznetsov and G. M. Zaslavsky, Phys. Rev. E **58**, 7330 (1998).
[16]F. Lekien, C. Coulliette, A. J. Mariano, E. H. Ryan, L. K. Shay, G. Haller, and J. Marsden, Physica D **210**, 1 (2005).
[17]J. Lundgren, http://www.mathworks.com/matlabcentral/fileexchange/28851-alpha-shapes for Alpha Shapes, MATLAB Central File Exchange, 2010; accessed February 2014.
[18]D. J. Muraki, C. Snyder, and R. Rotunno, J. Atmos. Sci. **56**, 1547 (1999).
[19]S. Newhouse and T. Pignataro, J. Stat. Phys. **72**, 1331 (1993).
[20]M. J. Olascoaga and G. Haller, Proc. Natl. Acad. Sci. **109**, 4738 (2012).
[21]T. Peacock and J. Dabiri, Chaos **20**, 017501 (2010).
[22]I. I. Rypina, L. J. Pratt, P. Wang, T. M. Özgökmen, and I. Mezić, Chaos **25**, 087401 (2015).
[23]H. A. Stone, A. D. Stroock, and A. Ajdari, Annu. Rev. Fluid Mech. **36**, 381 (2004).
[24]M. H. M. Sulman, H. S. Huntley, B. L. Lipphardt, Jr., and A. D. Kirwan, Jr., Physica D **258**, 77 (2013).
[25]J.-L. Thiffeault, Chaos **20**, 017516 (2010).
[26]J.-L. Thiffeault and M. Budisic, "Braidlab: A software package for braids and loops," e-print arXiv:1410.0849.
[27]M. R. Turner and M. A. Berger, Fluid Dyn. Res. **43**, 035501 (2011).
[28]G. K. Vallis, *Atmospheric and Oceanic Fluid Dynamics* (Cambridge University Press, 2006).
[29]P. Welander, Tellus **7**, 141 (1955).
[30]C. M. White, R. R. Steeper, and A. E. Lutz, Int. J. Hydrogen Energy **31**, 1292 (2006).